The Journal of Chemical Physics

RESEARCH ARTICLE | APRIL 09 2025

Computing photodissociation cross sections and quasi-continuum properties of the NH radical

Tereza Uhlíková; Sergei N. Yurchenko ; Armando N. Perri ; Jonathan Tennyson ; Gap-Sue Kim

J. Chem. Phys. 162, 144108 (2025)
https://doi.org/10.1063/5.0262447

AIP Publishing

The Journal of Chemical Physics ARTICLE pubs.aip.org/aip/jcp

Computing photodissociation cross sections and quasi-continuum properties of the NH radical

Cite as: J. Chem. Phys. 162, 144108 (2025); doi: 10.1063/5.0262447
Submitted: 1 February 2025 • Accepted: 21 March 2025 •
Published Online: 9 April 2025

Tereza Uhlíková,[1,a)] Sergei N. Yurchenko,[2,b)] Armando N. Perri,[2] Jonathan Tennyson,[2] and Gap-Sue Kim[3]

AFFILIATIONS

[1] Department of Analytical Chemistry, University of Chemistry and Technology, Technická 6, Prague, Czech Republic
[2] Department of Physics and Astronomy, University College London, WC1E 6BT London, United Kingdom
[3] Dharma College, Dongguk University, 30, Pildong-ro 1-gil, Jung-gu, Seoul 04620, South Korea

[a)] Electronic mail: tereza.uhlikova@vscht.cz
[b)] Author to whom correspondence should be addressed: s.yurchenko@ucl.ac.uk

ABSTRACT

Photodissociation cross sections of NH for $250 > \lambda > 100$ nm are studied using (i) the recently reported spectroscopic model of the five lowest electronic states of NH, (ii) a new set of *ab initio* potential energy, (transition) dipole moment, spin–orbit, and electronic angular momentum curves covering the region up to 100 000 cm^{-1}, and (iii) the recently suggested approach for time-independent calculations of continuum spectra of molecules (Pezzella *et al.*, 2022). Quasi-dissociative properties, including predissociation lifetimes and linewidths, of the $c^1\Pi$ state are studied using four state-of-the-art predissociative methods: stabilization, Airy-boundary conditions within the WKB approximation, phase–amplitude, and complex-scaling approaches. The methodologies developed and tested in this work will be used to produce photoabsorption and photodissociation spectra of NH and other diatomic species as part of the ExoMol database (Q.-H. Ni *et al.*, 2025) at www.exomol.com.

I. INTRODUCTION

Studies of the imidogen (NH) radical go back to the nineteenth century. Out of numerous spectroscopic studies published about imidogen, here only the most relevant papers are mentioned. For instance, the first observation of its $A\,^3\Pi$–$X\,^3\Sigma^-$ electronic transitions was reported by Eder[1] already in 1893. One of the first *ab initio* studies was performed by Boyd[2] in 1958, who studied the six lowest electronic states by solving the Roothaan equations. Meanwhile, one of the most recent experimental studies of NH from 2022 is the work by Pastorek *et al.*[3] on the time-resolved Fourier transform infrared emission of NH in its ground electronic state. A review of high-resolution spectroscopic studies of NH is provided by Darby-Lewis *et al.*[4] with a more general review of the infrared spectra of small radicals for exoplanetary spectroscopy can be found in Civiš *et al.*[5]

Most studies of electronic spectra of NH have focused on the $A^3\Pi$–$X\,^3\Sigma^-$ band system. Astronomically, A–X transitions were detected in Comet Cunningham[6] and Comet C/1996 B2 (Hyakutake),[7] observed in the interstellar medium toward the stars HD 27778 and HD 24398 by Meyer and Roth[8] and again in 1997 toward the star HD 149757 by Crawford and Williams.[9] Experimentally, molecular constants for this band were determined by Ram *et al.*[10] and later revised by Ram and Bernath.[11] An extensive new line list of rovibronic (rotational–vibrational–electronic) transitions has recently been calculated by Fernando *et al.*,[12] followed by Gupta *et al.*,[13] who performed an experimental study of the vibrationally resolved excitation of NH by electron-impact. In 2020, the photodissociation spectrum of the A–X system was studied using intense VUV pulses and the kinetic energy release method by Liu *et al.*[14]

More complex (*ab initio*) studies that involve other electronic states and interactions between them were presented, for instance,

by Yarkony,[15] Song *et al.*,[16] Zhang *et al.*,[17] and Zhou and Zhu.[18] Higher electronic states were the focus of a study by Owono Owono *et al.*[19] These authors calculated potential energy curves, spectroscopic constants, and dipole moment functions of the excited and Rydberg states of NH lying in the range of 11 eV (90 000 cm^{-1}) above the dissociation energy of the ground electronic ground state. Photoabsorption properties of NH between triplet states were studied *ab initio* by Kirby and Goldfield[20] and Owono Owono *et al.*,[21] who computed oscillator strengths, photodissociation cross sections, and rates.

The most comprehensive study of the rovibronic spectra of NH is the recent work by Perri and McKemmish,[22] who produced an accurate empirical model describing the five lowest electronic states $X\,^3\Sigma^-$, $a\,^1\Delta$, $A\,^3\Pi$, $b\,^1\Sigma^+$, and $c\,^1\Pi$. The spectroscopic model comprises *ab initio* potential energy, coupling (e.g., spin–orbit and angular momenta), and (transition) dipole moment curves, with some of the curves refined to experimental data from a previous MARVEL (Measured Active Rotational–Vibrational Energy Levels) study[4] for the $X\,^3\Sigma^-$, $a\,^1\Delta$, and $A\,^3\Pi$ electronic states. This model was used to generate an extensive and accurate line list for NH, called kNigHt, through rovibronic calculations performed using the diatomic variational nuclear-motion code Duo.[23] The "trihybrid" kNigHt line list includes energies obtained using three methodologies:[24] energies calculated with Duo, experimentally derived (MARVEL) energies from Darby-Lewis *et al.*,[4] and effective Hamiltonian energies from Brooke *et al.*[25,26] and Fernando *et al.*[12] The latter two sources were explicitly included to ensure accuracy alongside the complementary completeness offered by the variational model. The line list was designed to be applicable for high temperatures covering frequencies below 47 500 cm^{-1} (or wavelengths above ~211 nm).

Despite numerous studies of NH, there are still gaps in both experimental and theoretical descriptions of its photoabsorption UV–Vis spectra. In the present study, we focus on extending the spectroscopic coverage of the kNigHt line list to the shorter wavelength (above ~110 nm or below ~90 000 cm^{-1}) by studying photoabsorption cross sections, both direct and via predissociation, of NH in this region. To this end, we also extend the spectroscopic model of Perri and McKemmish[22] by computing higher excited electronic states lying above 50 000 cm^{-1} and using the program Duo[23] to evaluate the photoabsorption cross sections of NH. Duo has been extensively used to calculate line lists for diatomic molecules as part of the ExoMol project.[27] Moreover, Pezzella *et al.*[28] recently extended Duo for the treatment of bound–continuum transitions, which has been utilized to calculate the photoabsorption cross sections of HCl and HF[29] and OH.[30] In this work, we thus apply the methodology of Pezzella *et al.*[28] to NH.

Obtaining accurate photoabsorption spectra in the far UV region is a complex process. Apart from finely gridded potential energy curves (PECs) for all states of interest, it requires interactions between numerous electronic states such as spin–orbit coupling curves (SOCs) and electronic angular momentum curves (EAMCs). Moreover, including full dipole moments (DMs) and transition dipole moments (TDMs) into intensity predictions provides more reliable results than the Franck–Condon approximation; this can be very important for high-resolution applications. Our model covers the twelve lowest electronic states and interactions between them. It is based on empirical and *ab initio* spectroscopic data. The description of the five lowest electronic states $X\,^3\Sigma^-$, $a\,^1\Delta$, $b\,^1\Sigma^+$, $A\,^3\Pi$, and $c\,^1\Pi$ is taken from the study by Perri and McKemmish,[22] where an accurate spectroscopic model of NH was constructed by fitting PECs, as well as interaction terms [SOCs, EAMCs, and Born–Oppenheimer breakdown (BOB) correction curves], to the corresponding experimentally derived energy values.[4] We use high level *ab initio* theory to compute all the curves required (PECs, TDMCs, SOCs, etc.) for the remaining seven electronic states we consider, namely $1\,^5\Sigma^-$, $2\,^3\Sigma^-$, $2\,^3\Sigma^+$, $1\,^1\Sigma^-$, $2\,^1\Pi$, $2\,^3\Pi$, and $1\,^3\Delta$.

As part of the predissociative properties of NH, we look into the predissociative dynamics of the $c^1\Pi$ electronic state. Predissociation can provide a significant route to dissociation in the near-threshold region and deserves more attention. The $c\,^1\Pi$ PEC has a shallow minimum followed by a barrier, which makes this state an interesting object for studying the resonance (or metastable) states and the associated spectral features. These states are sensitive to the shape of the PECs and the magnitudes of the various interactions and can cause both radiative association and predissociation. There are numerous techniques and approaches in the literature designed to study resonances.[31–38]

The main objective of this study is to identify a suitable procedure to augment the direct photodissociation methodology of Pezzella *et al.*[28] Using a refined $c\,^1\Pi$ PEC from the kNigHt spectroscopic model, resonance state characterization is explored using four distinct techniques: (i) stabilization technique, where resonances are found as invariant, i.e., energetically stable states with varying box sizes;[33] (ii) Airy function boundary conditions as it is implemented in the widely used LEVEL16 program;[34] (iii) phase–amplitude method, where resonances appear as a jump in the phase;[36] and (iv) complex scaling method as a representative of non-Hermitian approaches.[37]

In summary, this study aims to achieve several objectives: to extend the spectroscopic model of kNigHt up to 90 000 cm^{-1}; to study the continuum photoabsorption cross sections of NH based on this model; and to investigate resonance states and the predissociation of NH within the $c\,^1\Pi$ electronic state.

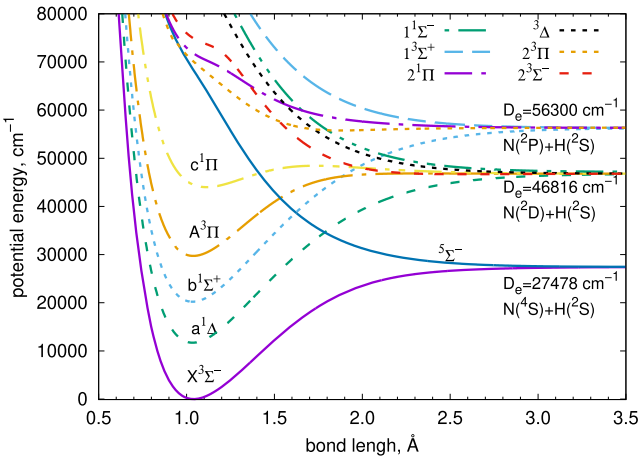

FIG. 1. Potential energy curves for the 12 lowest electronic states of NH included in the model. The five lowest PECs are taken from Perri and McKemmish.[22] The rest are based on high-level *ab initio* calculations using the MRCI/AV5Z method.

II. SPECTROSCOPIC MODEL

In the present work, we consider the 12 lowest electronic states of NH. For the lowest five states $X\,^3\Sigma^-$, $a\,^1\Delta$, $b\,^1\Sigma^+$, $A\,^3\Pi$, and $c\,^1\Pi$, the empirical spectroscopic model recently developed by Perri and McKemmish[22] is used. The remaining seven electronic states and all associated curves (PECs, SOCs, EAMCs, and TDMs) were computed *ab initio* as part of this work using the MOLPRO program package[39] employing the complete active space self-consistent field (CASSCF) approach and followed by an internally contracted multi-reference configuration interaction (icMRCI) calculations. With the correlation-consistent augmented cc-AV5Z Dunning basis set,[40] the full active space consisted of 3σ and 1π orbitals with only two electrons taken in the core. The states with the same symmetry were calculated together; otherwise, the calculations of different states proceeded individually. When calculating the excitation energies, a generalized Davidson correction was employed.

The potential energy curves for the 12 lowest electronic states of NH included in our spectroscopic model are displayed in Fig. 1. The five lowest PECs are from Perri and McKemmish,[22] and the rest are from our MRCI/AV5Z calculations. The first Rydberg states start just above the region covered in this work, at around 9.98 eV.[19] The properties and interaction curves are displayed in the following figures in this order: Fig. 2 shows 12 dipole moment curves and 13 electronic angular moment curves, Fig. 3 shows 32 spin–orbit coupling curves, and Fig. 4 shows 17 transition dipole moment curves.

A. Obtaining the rovibronic spectrum

We use the program Duo to solve a system of coupled Schrödinger equations for the 12 lowest electronic states of ^{14}NH. To obtain converged results, we used a box size of L = 19.5 Å covering bond lengths from r = 0.5 to 20 Å. Duo is a bound rovibronic solver; it solves the coupled Schrödinger equations variationally using bound vibrational basis functions regardless if the associated electronic states are bound or repulsive. Duo first solves the pure vibrational problems for the 12 electronic states independently using the sinc-DVR method[41] with all couplings ignored. The resulting vibrational eigenfunctions are then utilized to construct rovibronic basis functions in Hund's case (a) representation. In this work, we

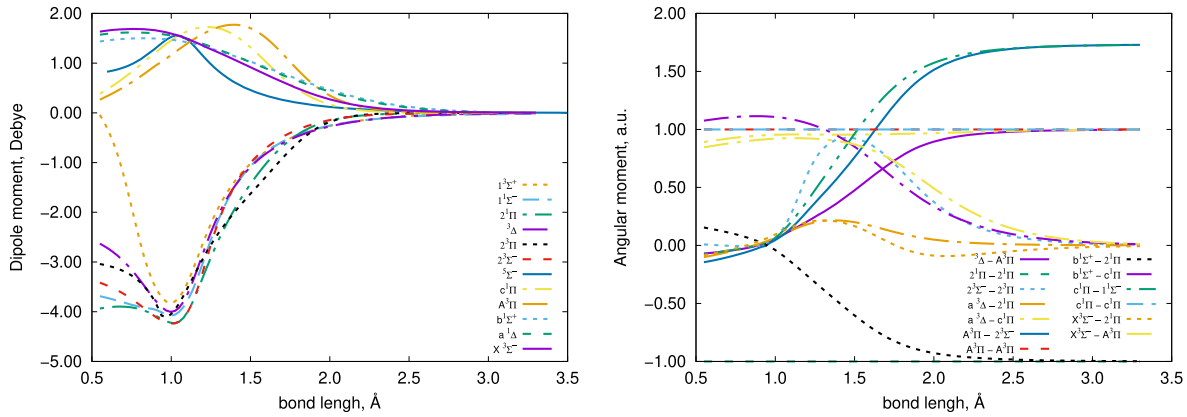

FIG. 2. Dipole moment functions (left panel) and angular momentum functions (right panel) for the 12 lowest electronic states of NH based on the high-level *ab initio* calculations using the MRCI/AV5Z method.

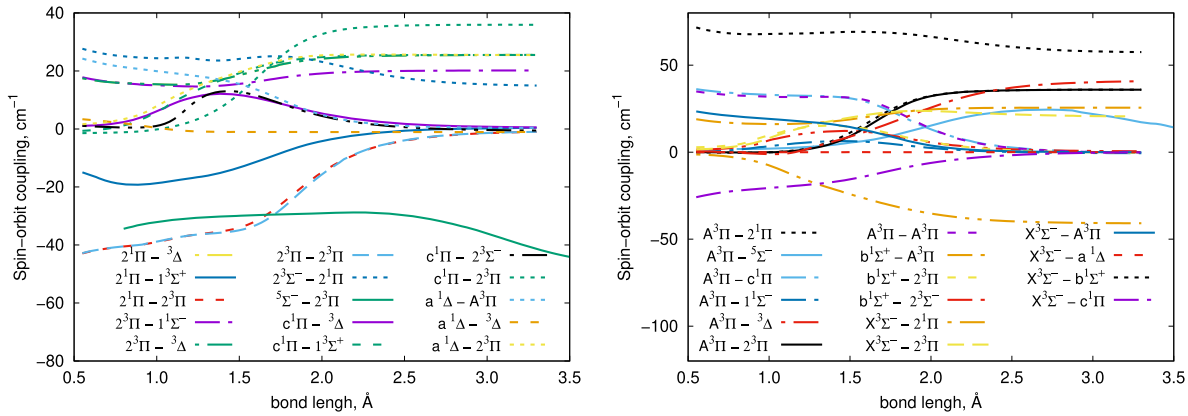

FIG. 3. Spin–orbit couplings between the 12 lowest electronic states of NH based on the high-level *ab initio* calculations using the MRCI/AV5Z method.

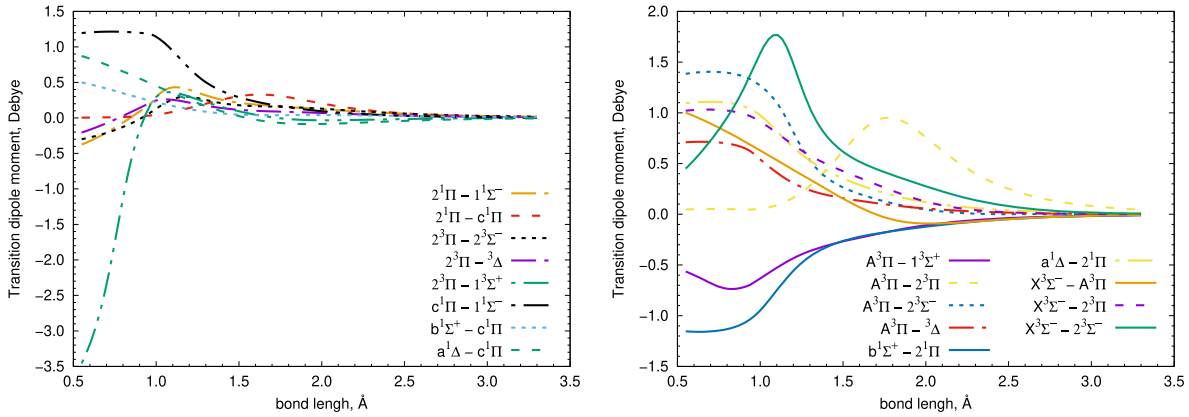

FIG. 4. Transition dipole moments between the 12 lowest electronic states of NH based on the high-level *ab initio* calculations using the MRCI/AV5Z method.

used the sinc-DVR method on a grid of 2001 points to represent the vibrational wavefunctions.

For the bound electronic states, i.e., $X\,^3\Sigma^-$, $a\,^1\Delta$, $b\,^1\Sigma^+$, $A\,^3\Pi$, and $c^1\Pi$, the vibrational basis sets are the true bound basis functions, vanishing at $r \to \infty$. We limit these to 30–40 functions for each bound electronic state. For the unbound electronic states, however, the vibrational basis function solutions are constructed to satisfy the boundary conditions of vanishing first derivatives exactly at the borders, rather than at $r \to \infty$. Therefore, in practice, these boundary conditions serve as a selection criterion that identifies a finite number of continuum states that provide a discretized representation of the continuum within the DUO box. This is illustrated in Fig. 5, where selected unbound wavefunctions of $2\,^3\Sigma^-$ and $2\,^3\Pi$ are shown as reduced densities together with their PECs. The size of the simulation box defines the density of the selected continuum states in the finite basis, while the number of sinc-DVR grid points provides the energy coverage. For each repulsive electronic state, we typically select 1000–2000 vibrational functions to represent the unbound vibrational basis set.

The full specification of the spectroscopic model can be found in the supplementary material in the form of a DUO input file.

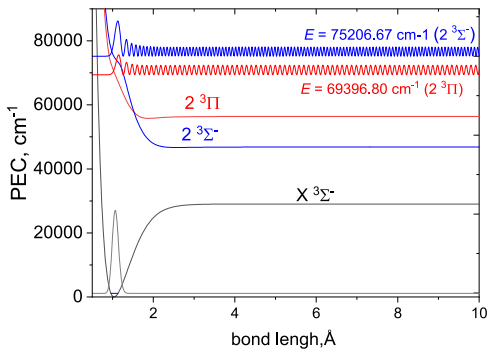

FIG. 5. PECs and selected wavefunctions (reduced densities) of $X\,^3\Sigma^-$, $2\,^3\Sigma^-$, and $2\,^3\Pi$.

III. CONTINUUM PHOTOABSORPTION CROSS SECTIONS

When computing the transition probabilities such as line strengths or Einstein coefficients, required for simulating spectra, DUO is capable of distinguishing the bound and continuum rovibronic states. This is done by analyzing radial densities of the corresponding wavefunctions: bound states vanish at long distances, while continuum states do not. We use this feature to process the bound and continuum states separately when computing intensities for transitions between different electronic states.[27]

After developing the full 12 electronic states of the NH spectroscopic model, one part of this study focuses directly on the continuum absorption spectrum in the range of 50 000–90 000 cm^{-1} (110–200 nm). There are two allowed electronic bands in this region, $2\,^3\Pi$–$X\,^3\Sigma^-$ and $2\,^3\Sigma^-$–$X\,^3\Sigma^-$, which are also the main absorbers. Transitions to the singlet states $a\,^1\Delta$, $b\,^1\Sigma^+$, $c\,^1\Pi$, $1\,^1\Sigma^-$, and $2\,^1\Pi$ and the pentet state $1\,^5\Sigma^-$ are forbidden and, therefore, can only contribute to the absorption through the couplings with $2\,^3\Pi$ and $2\,^3\Sigma^-$.

DUO treats the continuum as a finite bound-like system and obtains unbound solution for a discrete number of states.[28] Hence, the continuum photodissociation spectrum in our approach is also discretized.

An absorption line intensity for the transition from a bound state i with the energy $\tilde{E}_i$, in thermal equilibrium at the temperature T, to the (unbound) state f with energy $\tilde{E}_f$ is given by (cgs units)

$$I(f \leftarrow i) = \frac{8\pi^3 10^{-36} \tilde{\nu}_{if}}{3hc} \frac{e^{-c_2 \frac{\tilde{E}_i}{T}}}{Q} \left[1 - e^{-c_2 \frac{\tilde{\nu}_{fi}}{T}}\right] S(f \leftarrow i), \quad (1)$$

where $\tilde{\nu} = (\tilde{E}_f - \tilde{E}_i)$ is the transition wavenumber in cm^{-1}, c is the speed of light in vacuum in cm/s, and c_2 is the second radiation constant (cm/K). Q is the partition function defined as

$$Q = \sum_j g_j \, e^{-c_2 \tilde{E}_j / T}, \quad (2)$$

with g_j being the total degeneracy of the rovibronic state j,

$$g_j = g_{\rm ns}^{(j)} J_j (J_j + 1), \tag{3}$$

in which $g_{\rm ns}^{(j)}$ is the nuclear-spin statistical weight, which equals 6 for ^{14}N^{1}H.

For the main two unbound triplet systems, 2 $^3\Pi$ and 2 $^3\Sigma^-$, we obtain 303 and 334 vibrational states, respectively, below 100 000 cm^{-1} (above 100 nm) for a box size of 19.5 Å. Figure 5 illustrates continuum wavefunctions of the 2 $^3\Pi$ and 2 $^3\Sigma^-$ states of NH. They display a typical plane wave shape at long range and with a spike at the potential wall at short range.

The DUO eigenfunctions, for both bound and unbound states, are normalized like bound wavefunctions by integration over the box range $[r_{\rm min} \ldots r_{\rm max}]$. As a result, the intensity of the true continuum cross sections $\sigma(\tilde{\nu})$ (cm^2/molecule) is collapsed into a discrete set of absorption coefficients (cm/molecule) as in Eq. (1). Here, we follow the approach suggested by Pezzella *et al.*[28] and redistribute the absorption intensities I_{if} in Eq. (1) into cross sections by applying a Gaussian smoothing with a line profile given by

$$f_{\tilde{\nu}_{fi},\alpha_{\rm G}}(\tilde{\nu}) = \sqrt{\frac{\ln 2}{\pi}} \frac{1}{\alpha_{\rm G}} \exp\left(-\frac{(\tilde{\nu} - \tilde{\nu}_{fi})^2 \ln 2}{\alpha_{\rm G}^2}\right), \tag{4}$$

where $\alpha_{\rm G}$ is the half-width at half-maximum (HWHM) and $\tilde{\nu}_{fi}$ is the line center. The value of $\alpha_{\rm G}$ is chosen based on the distance between discretized transition frequencies such that the gaps between them are smoothly covered, see Yurchenko *et al.*,[42] and is typically of the order of 100–200 cm^{-1}.

It should be noted that the method of discretization of continuum was proposed by Reinhardt,[43] who demonstrated its equivalence to using quadratures when computing integrated cross sections.

A. Particle-in-a-box analogy

The method of Pezzella *et al.*[28] involves smoothing with a Gaussian function of constant width, $\alpha_{\rm G}$, whose choice is somewhat arbitrary. Pezzella *et al.*[44] recognized that there was an issue with using a constant width at higher energies and explored the idea of using a variable width. Here, we propose a method for choosing $\alpha_{\rm G}$, whose value and variation with energy are uniquely defined by the box size.

The continuum solution in DUO obtained with the infinite wall boundary conditions as imposed by the sinc-DVR basis functions can be compared to the particle in a box solution with the energies (in cm^{-1}) given by

$$\tilde{E}_n^{\rm box} = \frac{hn^2}{8\mu L^2 c}, \tag{5}$$

where μ is the reduced mass, L is the box size (Å), and $n \geq 1$ is the state counting number. The separation between states is, therefore, a linear function of n,

$$\Delta\tilde{E}_n^{\rm box} = \tilde{E}_{n+1}^{\rm box} - \tilde{E}_n^{\rm box} = \frac{h(2n+1)}{8\mu L^2 c}. \tag{6}$$

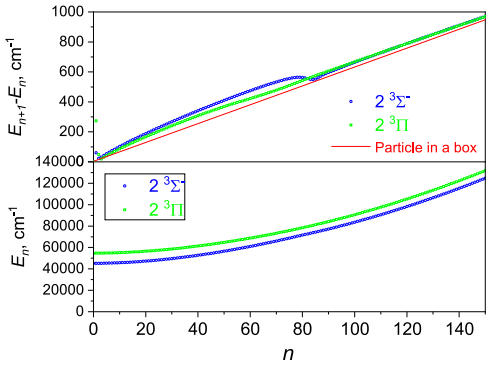

FIG. 6. Separation between the continuum states of 2 $^3\Sigma^-$ and 2 $^3\Pi$ and of the particle in a box computed for the same values of the reduced mass μ of NH and of the box size L = 7.5 Å.

In Fig. 6 (top panel), we compare the energy separations obtained for the 2 $^3\Pi$ and 2 $^3\Sigma^-$ states of NH to that of a particle in a box corresponding to μ of NH. A smaller size of the box L = 7.5 Å is chosen for illustration purposes. The corresponding energies are also shown (bottom panel). The separation curves are found to almost coincide with the particle in a box curve. Due to the linear dependence on n, there is no single optimal value of $\alpha_{\rm G}$ for the entire region. We, therefore, define $\alpha_{\rm G}$ to be $\Delta\tilde{E}_n^{\rm box}$ as in Eq. (6). This is now implemented in the code EXOCROSS,[45] which is used for intensity and cross section calculations here. In the current implementation, the selection of $\alpha_{\rm G}$ is based on the counting number n. Mitev *et al.*[30] used a similar methodology with $\alpha_{\rm G}$ as a function of the particle-in-the-box separation energy $\Delta\tilde{E}_n^{\rm box}$.

Figure 7 shows absorption line intensities computed using Eq. (1) for all transitions to 2 $^3\Sigma^-$ (f) from X $^3\Sigma_1^-$ ($\Omega'' = 1$), $v'' = 0$ for T = 1000 K using L = 7.5 Å. The separation between them varies from 400 to 600 cm^{-1}. The curves were obtained by re-distributing the discrete line intensities in Eq. (1) using a Gaussian function in Eq. (4) with HWHM $\alpha_{\rm G}$ estimated using Eq. (6).

B. Photoabsorption cross sections

The spectrum of NH in the ultraviolet region is dominated by overlapping direct photodissociative features from the unbound 2 $^3\Pi$ and 2 $^3\Sigma^-$ states centered at 140 nm. *Ab initio* cross sections for these two photodissociation processes were calculated for T = 0 K by Kirby and Goldfield.[20] There is also a photoabsorption feature at 300–350 nm due to transitions to the A $^3\Pi$ state. This state undergoes predissociation induced by the 1 $^5\Sigma^-$ state, which has been studied by Smith *et al.*[46] and Patel-Misra *et al.*[47] through lifetime analyses and subsequently modeled without a rotational structure by Heays *et al.*[48] These *ab initio* cross sections are collated in the Leiden Observatory photodissociation and photoionization database,[48,49] in addition to an *ad hoc* broad feature at 100 nm to account for processes involving higher electronic states.

Here, we model the direct photoabsorption processes of NH with a box size of 19.5 Å (r = [0.5 ... 20] Å) using 2001 sinc-DVR points for the integration grid. The number of vibrational states selected for the bound states are 40, 30, 30, and 40, while the

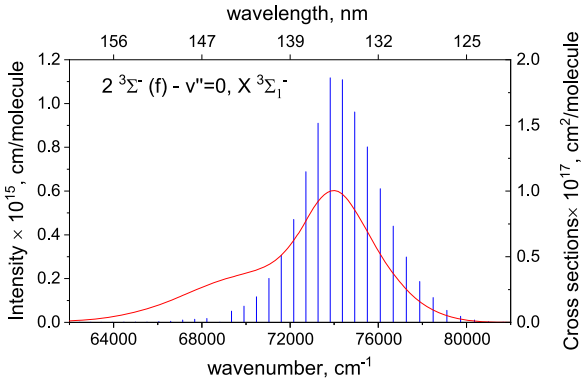

FIG. 7. Continuum spectrum $2\,^3\Sigma^-$ (f) ← $X\,^3\Sigma_1^-$, $v'' = 0$ of NH at $T = 1000$ K. Blue sticks: discrete "line intensities" illustrating the density of the discretized spectral lines. Red line: continuum cross sections obtained by distributing the discrete line intensities in Eq. (1) using Gaussian functions in Eq. (4) with HWHM α_G computed using Eq. (6).

unbound states $2\,^3\Pi$ and $2\,^3\Sigma^-$ are represented by 1000 vibrational basis functions. Using energies and Einstein A coefficients for all allowed transitions within 12 electronic states, the photoabsorption cross sections of NH were computed using the procedure established in Pezzella *et al.*[28] An example of cross sections of NH for $T = 300$ K is presented in Fig. 8 (left panel), showing the individual contributions of the $2\,^3\Sigma^-$ and $2\,^3\Pi$ bands to the total continuum spectrum of NH. The photoabsorption cross sections of continuum states manifest as exceptionally broad bands, underscoring the diverse nature of transitions occurring within the molecular system.

Figure 8 (right panel) offers a comparison of our cross sections with the cross sections of Kirby and Goldfield[20] for $T = 0$ K. Our cross sections show a redshift for both bands. The difference is because the difference in the positions of the bands should be due to the difference in *ab initio* methods used; we, therefore, believe that our results are more accurate. However, to the best of our knowledge, there are no experimental spectra of NH in this region to validate our predictions.

IV. RESONANCE STATES AND PREDISSOCIATION OF $c\,^1\Pi$

The $c\,^1\Pi$ state is different from $2\,^3\Sigma^-$ and $2\,^3\Pi$; in addition to the continuum region above its low-lying dissociation and shallow minimum, it is also characterized by a small barrier, leading to the formation of metastable rovibronic states known as shape resonances. These predissociating states, which lie energetically close to the level of this small hump, have shorter lifetimes, and the associated transition lines are broadened. In this section, the predissociation lifetimes and widths of $c\,^1\Pi$ are studied in detail.

A. Improving the $c\,^1\Pi$ PEC

The original line list kNigHt for NH was based on an *ab initio* PEC of the $c\,^1\Pi$ with an empirical shift.[22] Although this PEC provides a reasonable qualitative description of its shape (see Fig. 9), it is not sufficiently accurate for high-resolution spectroscopic applications. In addition, the kNigHt line list only included a few $c\,^1\Pi$ state levels lying below the energy threshold of 47 500 cm^{-1}.

For this work, we decided to refine the $c\,^1\Pi$ model to the experimental (MARVEL) energies. To this end, the following "diabatic" 2×2 analytic model was used to construct a shallow PEC of $c\,^1\Pi$ with a small barrier,[42,50]

$$\mathbf{A} = \begin{pmatrix} V_1(r) & W(r) \\ W(r) & V_2(r) \end{pmatrix}. \tag{7}$$

An EMO (Extended Morse Oscillator) function[51] was used for the diabatic PEC $V_1(r)$ as given by

$$V_1(r) = V_e + (A_e - V_e)\left[1 - \exp\left(-\sum_{k=0}^{N} B_k \xi_p^k (r - r_e)\right)\right]^2, \tag{8}$$

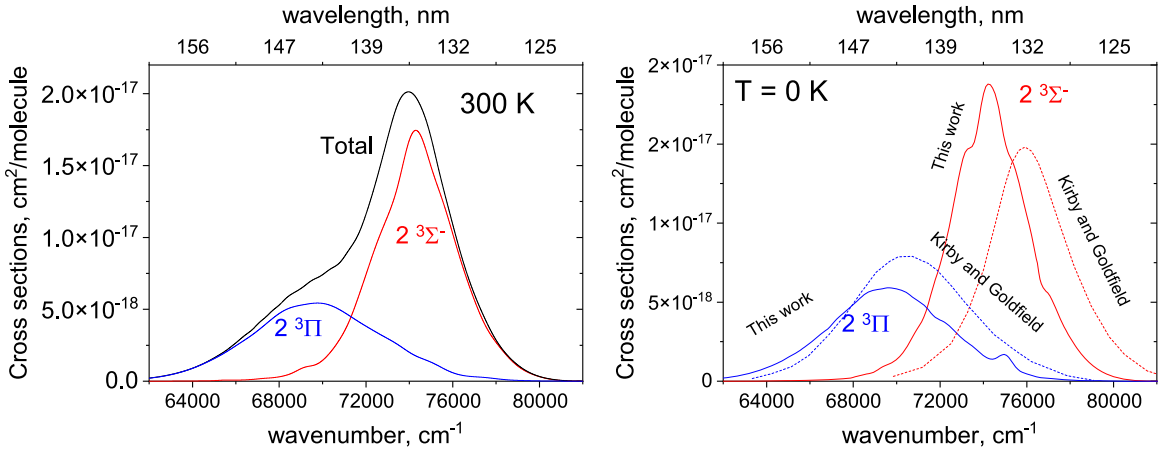

FIG. 8. Left panel: Continuum cross sections of NH (all states) for $L = 19.5$ Å obtained by distributing the discrete line intensities in Eq. (1) using a Gaussian profile in Eq. (4) with HWHM α_G from Eq. (6) showing contributions from the $2\,^3\Sigma^-$ and $2\,^3\Pi$ bands as well as the total continuum spectrum of NH at $T = 300$ K. Right panel: Computed absorption cross sections of the triplet system of NH at 140 nm at zero temperature showing comparison of this work with the previous calculations by Kirby and Goldfield.[20]

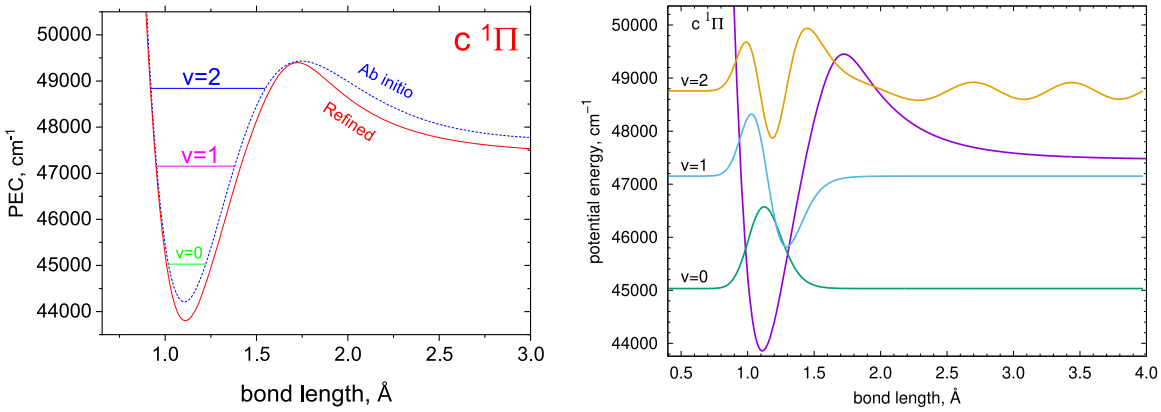

FIG. 9. Left panel: Comparison of the kNigHt $c\,^1\Pi$ PEC (*ab initio* calculated by the MRCI/AV5Z method with the T_e value adjusted[22]) and our refined PEC together with the $c\,^1\Pi$ vibrational levels. Right panel: Bound and resonant vibrational wavefunctions for the three lowest vibrational states of $c\,^1\Pi$ of NH in the rotationless ($J = 0$) limit.

where A_e is the dissociation asymptote, $A_e - V_e$ is the dissociation energy, r_e is the equilibrium distance of the diabatic PEC, and ξ_p is the Šurkus variable given by

$$\xi_p = \frac{r^p - r_e^p}{r^p + r_e^p}. \tag{9}$$

$V_2(r)$ in Eq. (7) was represented by a repulsive curve,

$$V_2(r) = A_e^A + \frac{a_6}{r^6}, \tag{10}$$

with A_e^A as an asymptote and played the role of a dummy state. The coupling curve $W(r)$ was modeled using an inverted EMO PEC with an asymptote of $W(r) \to 0$ at $r \to \infty$,

$$W(r) = W_0 - W_0[1 - \exp(-w_0(r - r_0))]^2. \tag{11}$$

The adiabatic $c\,^1\Pi$ PEC is then constructed as the lower eigenvalue of the diabatic matrix **A**, and the upper component is disregarded.

Apart from the $c^1\Pi$ PEC, we also refined the following curves associated with this state from the original kNigHt model: the Born–Oppenheimer Breakdown (BOB) correction and the EAMC (also called L-uncoupling) between $c\,^1\Pi$ and $b\,^1\Sigma^+$. The latter was necessary to recover the Λ-doubling in the $c\,^1\Pi$ energies. The new spectroscopic model is given in the supplementary material.

We have also extended the MARVEL energies of Darby-Lewis *et al.*[4] to include the $v = 2$ transitions from Graham and Lew.[52] These transitions came from unpublished measurements by Herzberg and were added to Graham and Lew[52] at the revision stage. The refined PEC and $v = 0, 1, 2$ energies of the $c^1\Pi$ state are illustrated in Fig. 9. The update MARVEL input file and MARVEL energy levels are also are given in the supplementary material.

B. Analysis

The $c^1\Pi$ PEC features a small hump with a height, in the case of our refined PEC, of 1945 cm^{-1} above the dissociation limit; see Fig. 9. Quantitatively, the $c\,^1\Pi$ state has a minimum at 43 809 cm^{-1}, dissociates at 47 455 cm^{-1}, and has its barrier peak at 49 400 cm^{-1}. Consequently, this potential barrier leads to the formation of so-called shape resonance states in the associated rovibrational wavefunctions. Resonance states are intriguing quantum entities that can act as gateways to initiate various molecular processes. Here, the tunneling predissociation lifetimes, which cause the vanishing of the NH spectral lines, are the focus of our interest. In the following, we look into some of these properties in detail using the refined $c\,^1\Pi$ PEC.

Experimentally, the $v = 0$ and $v = 1$ vibrational states are observed to predissociate starting from the rotational quantum numbers $J = 22$ and $J = 15$, respectively. The resonance effects in these states were characterized by Graham and Lew[52] and Brazier *et al.*,[53] where the associated linewidths were observed to increase until merging into the continuum and disappearing. Rotationally resolved transitions to the $v = 2$ state were reported only once, in 1978, by Dabrowski and Herzberg in the 2–0 band of the c–a system up to $J' = 6$, mentioned as a "Note added in proof" by Graham and Lew.[52] In the same study, mainly oriented on the d–c system, the $v'' = 2$ lines, except for $J'' = 1$, become increasingly diffuse and are not visible for $J > 5$ within this d–c system. Note, that the $d\,^1\Sigma^+$ electronic state lies above the region of interest for the present study.

In this study, the predissociations of the $c\,^1\Pi$ vibronic states are investigated theoretically using the following four different approaches: (1) stabilization technique, (2) Airy-function boundary condition, (3) phase–amplitude approach, and (4) complex-scaling method. The main ideas of these methods are briefly described below.

C. Stabilization method

The stabilization technique is well described by Mandelshtam *et al.*[33] The idea is to put an unbound system in a box of size L with infinite walls placed well outside the potential energy well and solve the resulting approximate Hamiltonian $\hat{H}$. This is usually done by imposing finite boundary conditions of vanishing density at the box border(s). The box size (i.e., the position of the infinite wall) is then gradually increased in order to reveal the differences between the

resonant and continuum states. Resonant states, once convergence is reached, should be "stable" for any further increase in the box size L. The continuum states, however, should behave like a textbook particle in a box solution, where the energies decrease as L^2, see Eq. (5), with plane wave like wavefunctions; see, e.g., Fig. 5. This approach has been used successfully to characterize predissociation via interaction with dissociative states;[38] here, we use it to look at shape resonances.

If the energy obtained by diagonalizing the Hamiltonian diagonalization remains unchanged with respect to variations in the box size, the state is considered stabilized, which reflects its bound nature. For fully bound states, the resulting energy remains constant for a given state. For quasi-bound states, deviations from the stabilized energy occur at certain box sizes, a phenomenon known as avoided crossing. This deviation can be interpreted as a spread around the stabilized energy, which, for quasi-bound states, determines the spectral linewidth—corresponding to the lifetime of the quasi-bound state.

To obtain the resonance positions of the energies and associated lifetimes, one needs to build and analyze the so-called stabilization diagram, representing the change in the eigenvalues with the change in box size L, on a grid of values of L. DUO was used to repeatedly solve the one-dimensional Schrödinger equation for the $c\,^1\Pi$ state using a series of enclosing boxes with varying box sizes $L : L_0 < L < L_0 + \Delta L$. Subsequently, a stabilization diagram for the $c^1\Pi$ energies as a function of L was constructed; see the left panel of Fig. 10. In this case, the box size L is presented as a internuclear distance r in Å, varied from 5.0 to 9.0 Å with a step of 0.01 Å. The density of states is then obtained by counting the number of states with energies between E and $E + \Delta E$ in the form of a histogram. It serves as a measure of the stability of a state (bound or quasi-bound). This density is then re-normalized by dividing the number of states for each energy channel by the total number of states in the used box. The resonance energy position ($E_{\rm res}$) and width (Γ) can be estimated by fitting each corresponding peak to the Lorentzian curve,[54]

$$\rho^{\rm res}(E) = \pi^{-1}\frac{\Gamma/2}{(E_{\rm res}-E)^2 + (\Gamma/2)^2}. \tag{12}$$

For our case of the $c\,^1\Pi$ state, the histogram (generated with ΔE equal to 0.5 cm^{-1}) is displayed in the right panel of Fig. 10. The six local maxima situated here are associated with the rotational state resonances of $J = 1$–6 for the vibrational state $v = 2$. The resulting energy positions for both bound and resonant rovibronic states are compiled in Table I. The corresponding widths (i.e., full width at half maximum, FWHM) of the resonant states are listed in Table II. Since the values in these tables are determined from a histogram generated with box size L varied from 5.0 to 9.0 Å using a step of 0.001 Å and $\Delta E = 10^{-6}$ cm^{-1}, resonance widths shorter than 10^{-6} cm^{-1} cannot be determined. However, for cases where $\tau_{\rm rad} \ll \tau_{\rm prediss}$, the value of $\tau_{\rm prediss}$ is not significant in determining the line broadening.

D. Airy function boundary condition method

In the widely used program LEVEL16,[34] tunneling lifetimes can be determined using Airy function boundary conditions at the outermost classical turning point, as introduced by Le Roy and Liu.[35] In general, LEVEL16 solves the radial Schrödinger equation on the basis of the Cooley–Cashion–Zare approach,[55–57] while for the metastable states that lie above the dissociation limit in a shallow potential well with a barrier to the dissociation (see Fig. 9, left panel), Airy function boundary conditions are applied. This approach as implemented in LEVEL16 was used to calculate predissociation lifetimes and predissociative widths for different J of $c\,^1\Pi$ of NH. The energy positions of bound and resonant rovibronic states, along with the corresponding widths for the resonant states, are presented in Tables I and II, respectively.

E. Phase–amplitude approach

The phase–amplitude (p–a) or phase-shift technique used in this study is described by Sidky and Ben-Itzhak.[36] In this approach, the solution of a one-dimensional Schrödinger equation is based on

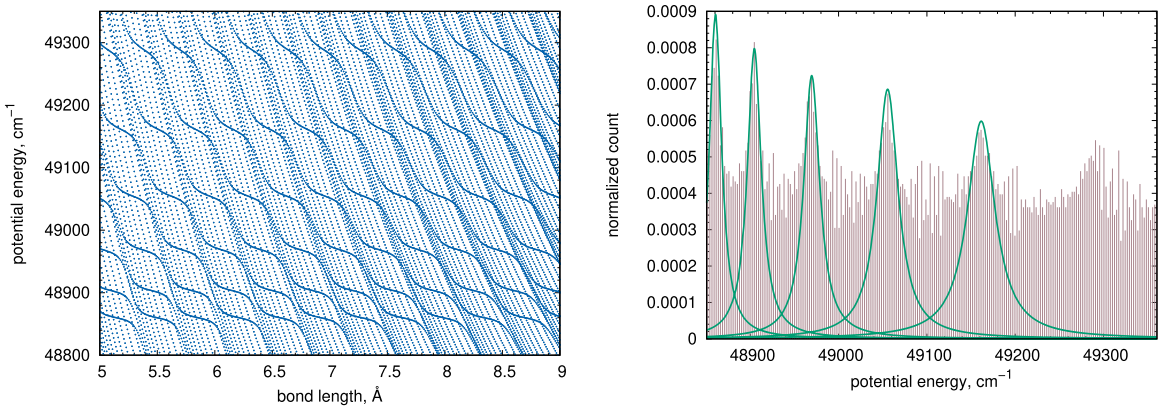

FIG. 10. Left: Part of a stabilization diagram for NH in its $c\,^1\Pi$ state, which covers the region of energies of the rotational states $J = 1$–6 within the vibrational state $v = 2$. Energies are calculated by DUO. Right: The corresponding histogram with Lorentzian fit green curves, see Eq. (12), of the particular rovibronic states. For instance, $v = 2$, $J = 4$ is localized at $E_{\rm res} = 49\,055$ cm^{-1} with $\Gamma = 29$ cm^{-1}.

TABLE I. The $c\,^1\Pi$ energy term values (in cm^{-1}) computed using the LEVEL16, stabilization (Duo), *p–a*, and *c-s* methods and using the refined kNigHt model are displayed. The energies are taken to the minimum of the $c\,^1\Pi$ potential curve.

v	J	LEVEL16	Stabil.	*p–a*	*c-s*	v	J	LEVEL16	Stabil.	*p–a*	*c-s*
0	1	1205.6	1205.9	1206.6	1206.7	1	1	3324.4	3326.0	3325.4	3325.7
0	2	1261.6	1262.0	1262.6	1262.3	1	2	3375.2	3376.9	3376.3	3376.2
0	3	1345.3	1345.8	1346.3	1346.1	1	3	3451.4	3453.1	3452.4	3452.3
0	4	1456.8	1457.3	1457.8	1457.6	1	4	3552.7	3554.4	3553.7	3553.6
0	5	1595.7	1596.2	1596.7	1596.5	1	5	3678.7	3680.5	3679.7	3679.6
0	6	1761.9	1762.4	1762.9	1762.7	1	6	3829.3	3831.3	3826.0	3830.2
0	7	1954.9	1955.5	1955.9	1955.7	1	7	4003.9	4005.8	4004.9	4004.8
0	8	2174.5	2175.3	2175.5	2175.2	1	8	4202.2	4204.1	4203.1	4203.0
0	9	2420.2	2420.9	2421.1	2421.9	1	9	4423.4	4425.7	4424.4	4424.3
0	10	2691.4	2692.3	2692.4	2692.2	1	10	4667.0	4669.3	4667.0	4667.9
0	11	2987.8	2988.8	2988.8	2988.5	1	11	4932.3	4936.0	4933.2	4933.2
0	12	3308.6	3311.1	3309.6	3309.0	1	12	5218.3	5220.5	5219.2	5218.8
0	13	3653.3	3654.5	3654.2	3653.3	1	13	5523.9	5525.2	5524.9	5524.6
0	14	4021.1	4021.7	4022.0	4021.7	1	14	5848.1	5851.6	5849.0	5848.4
0	15	4411.1	4412.7	4412.0	4411.7	1	15	6189.4	6192.9	6190.3	6189.6
0	16	4822.6	4824.1	4823.5	4823.2	1	16	6546.1	6549.2	6546.9	6542.9
0	17	5254.5	5256.8	5255.4	5255.2	1	17	6916.4	6920.8	6917.4	6916.2
0	18	5705.8	5708.0	5706.7	5706.2	1	18	7298.7	7300.8	7300.0	7299.3
0	19	6175.3	6178.4	6176.2	6175.2						
0	20	6661.7	6663.7	6662.5	6662.1	2	1	5012.2	5013.5	5013.0	5012.9
0	21	7163.3	7165.3	7164.1	7163.8	2	2	5055.7	5056.2	5056.3	5052.5
0	22	7678.3	7680.5	7679.1	7678.7	2	3	5120.7	5121.8	5121.3	5120.9
0	23	8204.4	8206.8	8205.3	8204.4	2	4	5206.8	5208.2	5207.6	5204.6
0	24	8739.0	8742.9	8739.8	8739.4	2	5	5313.7	5313.7	5314.6	5312.5
0	25	9278.9	9281.9	9280.6	9279.9						

the modified semi-classical Milne approach,[58] which represents the wavefunction as a variable amplitude $\alpha(r)$ multiplied by the sine of a variable phase $\phi(r)$, given by

$$\psi = \sqrt{\frac{2\mu}{\pi}} \exp\, \alpha(r) \sin\, \phi(r). \tag{13}$$

This approach takes advantage of the property of the phase, which changes smoothly as a function of energy, until a bound or resonance state is encountered. At this point, the phase exhibits a jump, which is illustrated in the left panel of Fig. 11, where the phase dependence to energy is shown for the refined NH $c\,^1\Pi$ state. The plot demonstrates two jumps corresponding to rovibrational states with quantum numbers $J = 8, v = 1$ and $J = 8, v = 2$. By taking the derivative of the phase with respect to energy, $\partial\phi(r,E)/\partial E$, the resonance energy position and width can be determined by fitting this derivative to the Lorentzian profile [Eq. (12)]. The results for the different rotational states with $J = 1$–5 within the vibrational state $v = 2$ are shown in the right panel of Fig. 11. Again, the resulting energy positions of the bound and resonant rovibronic states, along with the corresponding widths for the resonant states, are presented in Tables I and II, respectively, with the results from the other approaches.

Apart from the calculation of energy positions and widths of the resonance states (see Tables I and II), we also used this method for visualization of quasi-bound wavefunctions. Figure 9 (right panel) shows vibrational wavefunctions of the three existing bound states of $c^1\Pi$. The two lowest wavefunctions are found to be perfectly bound and localized inside the potential well with energies $E_{v=0} = 45\,050$ cm^{-1} and $E_{v=1} = 47\,170$ cm^{-1}. Conversely, in the third vibronic state ($v = 2$), with an energy level close to the barrier height $E_{v=2} = 48\,814$ cm^{-1}, the eigenfunction looks like a slightly deformed wavefunction of a free particle.

F. Complex-scaling approach

For our final method of locating resonance states, we employ a representative of the non-Hermitian techniques, the complex-scaling approach (*c-s*). This was originally introduced for locating resonances as poles of the S matrix in quantum two-particle collision processes.[59] Two-particle collision processes can lead to the formation of a species (reaction product) by emitting light, a phenomenon known as radiative association, which is the reverse process to our study of predissociation. Here, we investigate if *c-s* is comparable with the aforementioned methods usually used in high-resolution spectroscopy. Spectroscopic applications of *c-s* include Baková *et al.*,[60] Šedivcová *et al.*,[61] and Šedivcová-Uhlíková *et al.*[62] with the experimental confirmation of results by Püttner *et al.*[63] and Jochim *et al.*[64,65]

A thorough mathematical description of the *c-s* approach can be found in the report by Moiseyev.[37] The core principle of *c-s* is to

TABLE II. $c^1\Pi$ predissociation widths γ_{prediss} (in cm^{-1}) calculated using the LEVEL16, stabilization, *p–a*, and *c-s* methods are collected. The corresponding predissociative lifetimes τ_{prediss} (in s) from the LEVEL16 approach and radiative lifetimes τ_{rad} (in s) from Duo calculated using the refined kNigHt model.

		Predissociative widths γ_{prediss} (cm^{-1})				Lifetimes τ (s)		
v	J	LEVEL16	Stabil.	*P–a*	*c-s*	$\tau_{\text{prediss}}^{\text{LEVEL}}$	τ_{rad}	τ_{total}
0	15	3×10^{-7}	$< \times 10^{-6}$	2×10^{-7}	$< \times 10^{-6}$	2.09×10^{-5}	6.84×10^{-7}	6.62×10^{-7}
0	16	9×10^{-6}	2×10^{-6}	9×10^{-6}	$< \times 10^{-6}$	5.89×10^{-7}	7.19×10^{-7}	3.23×10^{-7}
0	17	1×10^{-4}	2×10^{-4}	1×10^{-4}	1×10^{-4}	4.06×10^{-8}	7.59×10^{-7}	3.85×10^{-8}
0	18	1×10^{-3}	1×10^{-3}	1×10^{-3}	7×10^{-3}	4.6×10^{-9}	8.09×10^{-7}	4.57×10^{-9}
0	19	7×10^{-3}	8×10^{-3}	8×10^{-3}	1×10^{-2}	7.18×10^{-10}	8.65×10^{-7}	7.17×10^{-10}
0	20	4×10^{-2}	5×10^{-2}	4×10^{-2}	2×10^{-2}	1.41×10^{-10}	9.35×10^{-7}	1.41×10^{-10}
0	21	2×10^{-1}	2×10^{-1}	2×10^{-1}	1×10^{-1}	3.29×10^{-11}	1.02×10^{-6}	3.29×10^{-11}
0	22	6×10^{-1}	2×10^{-1}	7×10^{-1}	4×10^{-1}	8.81×10^{-12}	1.13×10^{-6}	8.81×10^{-12}
0	23	2	4	2	1	2.68×10^{-12}	1.35×10^{-6}	2.68×10^{-12}
0	24	6	6	7	4	9.11×10^{-13}	1.5×10^{-6}	9.11×10^{-13}
0	25	15	21	17	9	3.5×10^{-13}	1.95×10^{-6}	3.5×10^{-13}
1	5	1×10^{-7}	$< \times 10^{-6}$	$< \times 10^{-8}$	$< \times 10^{-6}$	3.79×10^{-5}	6.21×10^{-7}	3.79×10^{-7}
1	6	6×10^{-6}	$< \times 10^{-6}$	$< \times 10^{-8}$	$< \times 10^{-6}$	8.93×10^{-7}	6.33×10^{-7}	6.11×10^{-7}
1	7	7×10^{-5}	3×10^{-5}	3×10^{-5}	5×10^{-6}	8.02×10^{-8}	6.47×10^{-7}	7.14×10^{-8}
1	8	4×10^{-4}	5×10^{-5}	4×10^{-4}	3×10^{-4}	1.19×10^{-8}	6.64×10^{-7}	1.17×10^{-8}
1	9	2×10^{-3}	3×10^{-3}	2×10^{-3}	4×10^{-4}	2.34×10^{-9}	6.94×10^{-7}	2.33×10^{-9}
1	10	1×10^{-2}	1×10^{-2}	1×10^{-2}	2×10^{-3}	5.55×10^{-10}	7.07×10^{-7}	5.55×10^{-10}
1	11	4×10^{-2}	5×10^{-2}	4×10^{-2}	4×10^{-2}	1.51×10^{-10}	7.35×10^{-7}	1.51×10^{-10}
1	12	1×10^{-1}	1×10^{-1}	1×10^{-1}	3×10^{-2}	4.58×10^{-11}	7.7×10^{-7}	4.58×10^{-11}
1	13	3×10^{-1}	3×10^{-1}	4×10^{-1}	2×10^{-1}	1.52×10^{-11}	8.08×10^{-7}	1.52×10^{-11}
1	14	1	2	1	6×10^{-1}	5.52×10^{-12}	9.62×10^{-7}	5.52×10^{-12}
1	15	2	3	3	1	2.15×10^{-12}	9.38×10^{-7}	2.15×10^{-12}
1	16	6	6	6	6	9.06×10^{-13}	1.02×10^{-6}	9.06×10^{-13}
1	17	13	14	14	7	4.11×10^{-13}	1.24×10^{-6}	4.11×10^{-13}
1	18	26	30	28	19	2.02×10^{-13}	1.3×10^{-6}	2.02×10^{-13}
2	1	10	7	10	4	5.55×10^{-13}	8.35×10^{-7}	5.55×10^{-13}
2	2	11	7	11	7	4.95×10^{-13}	8.45×10^{-7}	4.95×10^{-13}
2	3	13	8	13	7	4.19×10^{-13}	8.72×10^{-7}	4.19×10^{-13}
2	4	16	10	16	8	3.39×10^{-13}	9.48×10^{-7}	3.39×10^{-13}

solve the vibrational Schrödinger equation using a complex coordinate. To this end, the operator $\hat{S}$ with the parameter θ is introduced as given by

$$\hat{S} = \exp\left(i\theta r \frac{\partial}{\partial r}\right), \tag{14}$$

where r is a coordinate representing the bond length in our case. When $\hat{S}$ acts on the Hamiltonian operator $\hat{H}$, it effectively rotates its coordinate axes into the complex plane as

$$\hat{S}\hat{H}(r) = \hat{H}(r \cdot e^{i\theta}). \tag{15}$$

Resonance states can be accurately characterized as the complex eigenvalues of the modified $\hat{H}$,

$$\hat{H}(r \cdot e^{i\theta})\phi_n^{\text{res}}(r \cdot e^{i\theta}) = E_n \phi_n^{\text{res}}(r \cdot e^{i\theta}), \tag{16}$$

which leads to eigenvalue energies,

$$E_n = \epsilon_n - (i/2)\Gamma_n, \tag{17}$$

where ϵ_n is the resonance position and Γ_n is the width of the resonance state. The predissociation lifetime is consequently determined according to the following formula:

$$\tau_n = \frac{1}{2\Gamma_n c\pi}, \tag{18}$$

where c is the speed of light in cm/s.

Note that the *c-s* method is based on an analytical transformation in coordinate space. This requires the potential energy curve to be an analytic function of the coordinates, which is not always the case. Nevertheless, various approaches have been proposed in the literature to overcome this limitation.[66,67] In this study, where the

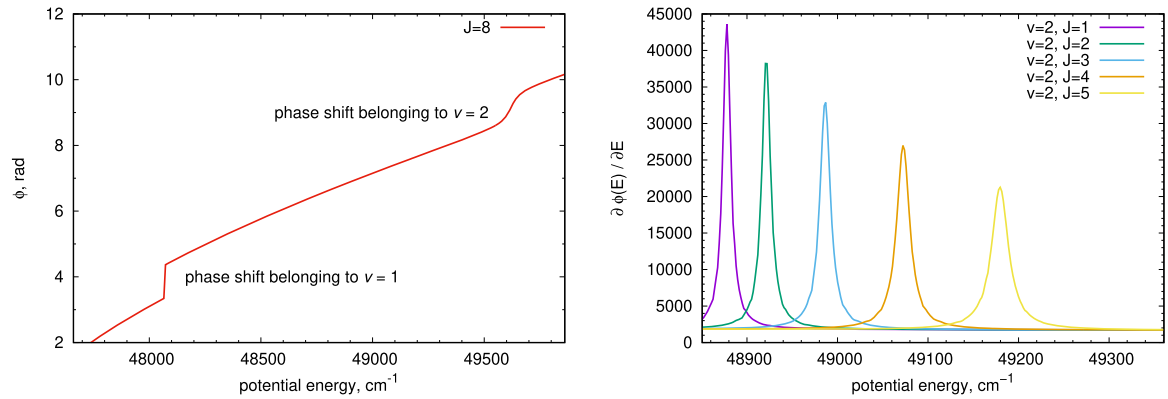

FIG. 11. Results of searching for a resonance state utilizing the *a–p* approach. Left: The phase as a function of the potential energy wavenumber for $J = 8$. The two jumps in the phase belong to the vibrational states $v = 1$ and $v = 2$. Right: The derivative of phase with respect to the energy, $\partial\phi(r, E)/\partial E$, for the most interesting vibrational state $v = 2$. The five resonance peaks for different quantum numbers J show the decreasing intensity and increasing widths of the resonance states. As an example, the state for $J = 1$ is located at $E_{res} = 48\,864$ cm^{-1} with $\Gamma = 10$ cm^{-1}.

$c\,^1\Pi$ PEC is represented by a grid, we use the technique based on the sinc-DVR basis set described by Mandelshtam and Moiseyev.[68]

The complex energy eigenvalues E_n (for the pure vibronic problem) computed using the complex-scaled Hamiltonian for the refined $c^1\Pi$ state are shown in Fig. 12 with the parameter θ varied from 0.0 to 0.03 rad in steps of 0.0005 rad. Each color belongs to a different value of θ. The $v = 2$ resonance state is clearly seen at the complex energy value $E = 48\,814 - 4.3i$ cm^{-1}. This corresponds to a predissociation lifetime of 10^{-6} μs. Similar to the stabilization approach, the calculations of the *c-s* energy positions and widths are performed using a numerical grid of the PEC with a step size of 0.2 Å and a grid for θ values with a step size of 10^{-6} rad. These parameters allow for the determination of widths greater than 10^{-6} cm^{-1}.

The sixth columns in Tables I and II belong to the resulting energy positions of bound and resonant rovibronic states and their corresponding widths for the resonant states.

G. Predissociative states and associated lifetimes of the $c^1\Pi$ state

The rovibronic energies of $c\,^1\Pi$ computed using different methods are collected in Table I, including the resonances of the quasi-bound states. For better comparison, the energies (in cm^{-1}) are taken relative to the minimum of the $c^1\Pi$ potential curve (43 809 cm^{-1}). The dissociation energy is then 3647 cm^{-1}, and the barrier height is 5592 cm^{-1}. All four methods provide similar results not

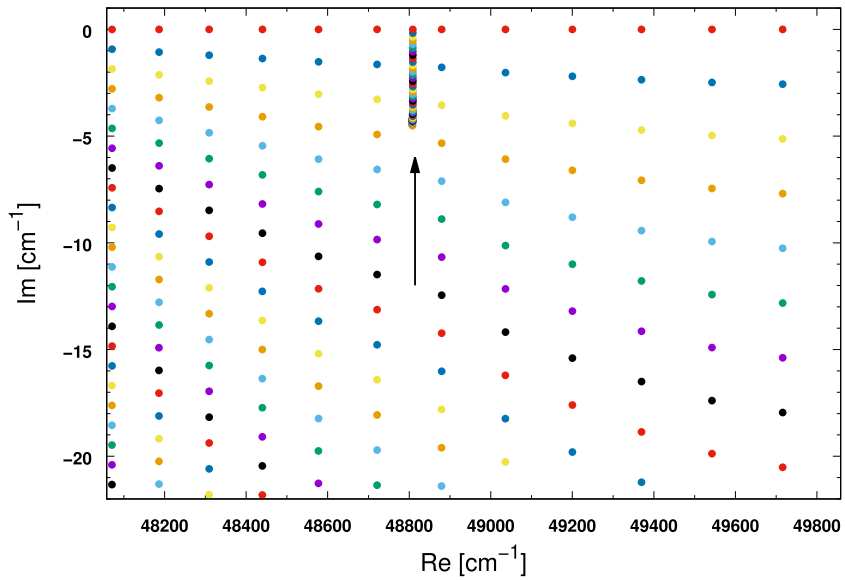

FIG. 12. Energy spectrum of the complex-scaled Hamiltonian of the NH $c\,^1\Pi$ state. The parameter θ is varied from 0.0 to 0.03 rad by the step-size of 5×10^{-4} rad. The resonance state is marked by an arrow and localized at 48 814 cm^{-1} with its width 4.3 cm^{-1}. Each set of point with the same color corresponds to the same θ value.

only for bound states but also for quasi-bound states. The rovibronic states above the dissociation limit are $J > 14$, $J > 6$, and all J for $v = 0$, $v = 1$, and $v = 2$, respectively. The corresponding predissociative widths Γ_{prediss} (FWHM) for quasi-bound states are summarized in Table II.

Even if the basis of the different methods used here for solving metastable states is very different, all of them provide very similar results in both energy positions and widths. In general, all methods confirm the presence of predissociative broadening in the $c^1\Pi$ spectrum due to the tunneling effect through the barrier in the $c^1\Pi$ PEC. The broadening should be observable for $J > 20$, $v = 0$; $J > 15$, $v = 1$; and all transitions belonging to $v = 2$. Our findings support the experimental results of Graham and Lew[52] about the visibility or in other words vanishing spectral features.

Each of the methods tested has its own advantages and disadvantages. LEVEL16 is widely used due to its well-established foundation in the WKB approximation and Numerov algorithm[55] for the numerical integration of the Schrödinger equation. However, this can be used only for one-dimensional potentials. In contrast, the stabilization technique employed here is based purely on an *ab initio* (or, where applicable, empirical) PEC, and the Hamiltonian is diagonalized in the sinc-DVR basis. A significant advantage of the stabilization technique is its applicability to both multi-dimensional problems and the determination of quasi-bound states above the dissociation limit, as well as photoabsorption cross sections in the continuum. The discrepancies in the results obtained using these two methods for the states studied fall within the error margins of the applied approximations or numerical solutions (e.g., fitting the state diagram with a Lorentzian function to determine the position and lifetime).

The *p–a* method is fundamentally similar to the approach implemented in the LEVEL16 program and is successfully used for the determination of extremely narrow spectral lines.[66] From Tables I and II, it is evident that only negligible differences exist between the results obtained with *p–a* and those from LEVEL16. However, *p–a* is limited to one-dimensional cases as well.

The *c-s* method exhibits the largest deviation in lifetime calculations from other three. While conceptually highly robust and even applicable to the solution of multidimensional coupled systems, its use has certain limitations. First, as was mentioned above, the *c-s* method requires the potential to be an analytic function of the coordinates, which needs to be carefully treated. Second, in its original form, the rotation of the entire coordinate range into the complex plane may result in a non-physical deformation of the rotated potential. To mitigate this issue, approximations such as complex absorption potentials[69,70] or exterior complex scaling[71] have been developed. Testing these approximations for lifetime calculations will be the subject of future research.

H. Final spectrum of $c^1\Pi$

The radiative lifetimes of the $c\,^1\Pi$ states reported in Table II can be used for simulating the realistic absorption spectra of the $c\,^1\Pi$–$X\,^3\Sigma^-$ band with lines broadened by predissociation. To this end, we first compute the radiative lifetimes from the Einstein A coefficients using the standard approach,

$$\tau_i^{\text{rad}} = \frac{1}{\sum_{j<i} A_{ij}}, \tag{19}$$

where the index j indicates states with energies lower than the energy of the state i and A_{ij} correspond to the bound–bound transition probabilities for all the bound states in the NH line list using Duo. We then select the LEVEL16 values of linewidths γ_{prediss} from Table II and obtain the predissociated lifetimes $\tau_{\text{prediss}}^{\text{LEVEL}}$ as

$$\tau_{\text{prediss}}^{\text{LEVEL}} = \frac{1}{2\pi c \gamma_{\text{prediss}}^{\text{LEVEL}}}.$$

Here, $\tau_{\text{prediss}}^{\text{LEVEL}}$ of $c\,^1\Pi$ were computed using our new empirical $c\,^1\Pi$ PEC. Finally, the radiative and predissociative lifetimes were combined to obtain the total lifetimes of $c\,^1\Pi$ as given by

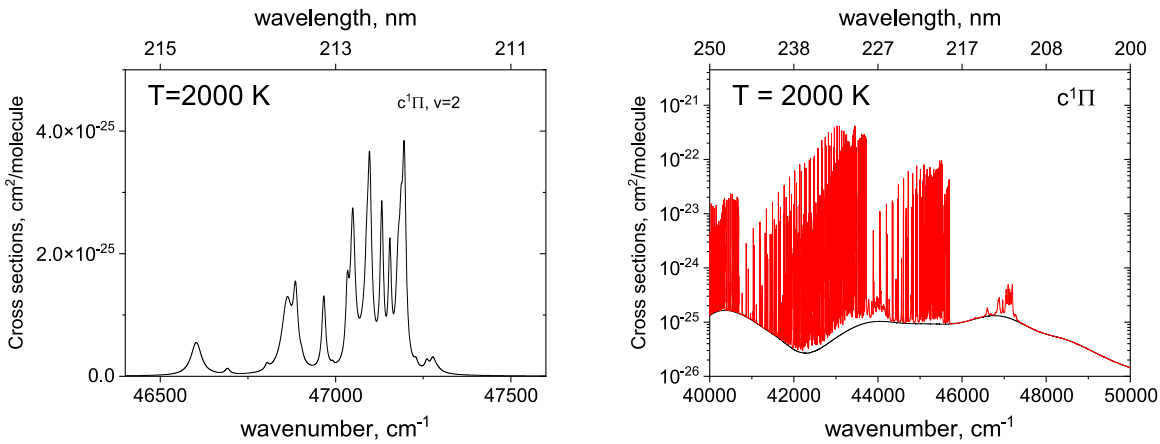

FIG. 13. Absorption cross sections for the rovibronic transition $c\,^1\Pi \leftarrow a\,^1\Delta$ electronic band. A refined kNigHt model was used to produce the line list, while the predissociative linewidths are from Table II. The featureless baseline in the right panel is a contribution from the bound–continuum transitions, while the sharp features (red lines) are formed by the bound–bound transitions.

$$\frac{1}{\tau_{\text{total}}} = \frac{1}{\tau_{\text{rad}}} + \frac{1}{\tau_{\text{prediss}}}, \tag{20}$$

also listed in Table II. For the overall accuracy of computed lifetimes with LEVEL16, it is assumed that the accuracy of the WKB-Airy function method is about 10% for resonances close to the dissociation limit with predissociation caused by tunneling through the potential barrier. We can expect similar uncertainties for the other methods.

Figure 13 illustrates the effect of the predissociative and dissociative treatment on the absorption cross sections of the $c\,^1\Pi$–$a\,^1\Delta$ band of NH. The left panel shows an absorption spectrum of the strongly predissociated $v = 2$ band at $T = 2000$ K simulated with ExoCross using the predissociative line broadening parameters from Table II (column $\tau^{\text{LEVEL}}_{\text{prediss}}$). The higher temperature is chosen to make the effect especially rich. The right panel shows the individual contributions to the NH photoabsorption spectra of $c\,^1\Pi$–$a\,^1\Delta$ from the bound–bound (sharp features) and bound–continuum transitions, with the latter forming a featureless baseline.

V. CONCLUSIONS

Our study is focused on the continuum absorption spectrum of NH in the range of 50 000–90 000 cm^{-1} (100–200 nm). This is based on the recently proposed methodology for computing photoabsorption cross sections,[28] which was extensively tested for the energies and Einstein A coefficients of NH computed with Duo for all allowed transitions within 12 electronic states. It was shown that the two electronic bands $2\,^3\Pi$–$X\,^3\Sigma^-$ and $2\,^3\Sigma^-$–$X\,^3\Sigma^-$ are the primary absorbers in the spectral region considered. Moreover, a new method based on the particle in a box solution was proposed for estimating the distance between the discretized bound–continuum transitions and associated the Gaussian widths as part of the continuum spectra simulations. Our continuum photoabsorption cross sections showed a redshift for both bands compared to previous theoretical work in the literature.

The predissociation lifetimes of the $c\,^1\Pi$ vibronic states were investigated using four different approaches. All four methods agree well in terms of both energies and lifetimes. The advantage of the stabilization and *c-s* approaches is that they are suitable for coupled multi-electronic state calculations. It would be especially interesting to include the *c-s* methodology into Duo, which will be the subject of future developments.

The methodologies tested and/or developed here will be used to produce temperature-dependent photoabsorption, photodissociation, and predissociation cross sections for NH to be included in the ExoMol database.[27,72] These results will also be used to update the kNigHt line list[22] using the newly computed predissociative spectrum of NH. Our recent studies have shown that the long-wavelengths (i.e., near-threshold) and the photodissociation cross section show a strong temperature dependence,[29] and our recent study of OH showed that, at least for this radical, predissociation also shows a strong temperature dependence.[30]

SUPPLEMENTARY MATERIAL

The supplementary material comprises the spectroscopic model of NH in the form of a Duo input file, which contains all curves, parameters, and experimentally derived energy term values of NH used in the fit. Our updated MARVEL input (transitions) file and output (energy levels) files are also given.

ACKNOWLEDGMENTS

This work was supported by the European Research Council (ERC) under the European Union's Horizon 2020 research and innovation program through Advance Grant No. 883830 and STFC Project No. ST/Y001508/1. The authors acknowledge the use of the DiRAC Data Intensive service (CSD3) at the University of Cambridge, managed by the University of Cambridge University Information Services and the DiRAC Data Intensive service (DIaL2) at the University of Leicester, managed by the University of Leicester Research Computing Service on behalf of the STFC DiRAC HPC Facility (www.dirac.ac.uk). The DiRAC services at Cambridge and Leicester were funded by BEIS, UKRI and STFC capital funding and STFC operation grants. T.U. acknowledges computational resources provided by the e-INFRA CZ project (ID: 90254), supported by the Ministry of Education, Youth and Sports of the Czech Republic, support from the Czech Science Foundation (GACR, Grant No. 24-12586S).

AUTHOR DECLARATIONS

Conflict of Interest

The authors have no conflicts to disclose.

Author Contributions

Tereza Uhlíková: Conceptualization (equal); Data curation (equal); Formal analysis (equal); Funding acquisition (equal); Investigation (equal); Methodology (equal); Project administration (equal); Resources (equal); Software (equal); Supervision (equal); Validation (equal); Visualization (equal); Writing – original draft (equal); Writing – review & editing (equal). **Sergei N. Yurchenko**: Conceptualization (equal); Data curation (equal); Formal analysis (equal); Funding acquisition (equal); Investigation (equal); Methodology (equal); Project administration (equal); Resources (equal); Software (equal); Supervision (equal); Validation (equal); Visualization (equal); Writing – original draft (equal); Writing – review & editing (equal). **Armando N. Perri**: Conceptualization (equal); Data curation (equal); Formal analysis (equal); Investigation (equal); Methodology (equal); Validation (equal); Visualization (equal); Writing – original draft (equal); Writing – review & editing (equal). **Jonathan Tennyson**: Conceptualization (equal); Data curation (equal); Formal analysis (equal); Funding acquisition (equal); Investigation (equal); Methodology (equal); Project administration (equal); Resources (equal); Software (equal); Supervision (equal); Validation (equal); Visualization (equal); Writing – original draft (equal); Writing – review & editing (equal). **Gap-Sue Kim**: Data curation (equal); Formal analysis (equal); Investigation (equal).

DATA AVAILABILITY

The data that support the findings of this study are available within the article and its supplementary material.

REFERENCES

[1] J. M. Eder, Wien Akad **60**, 1 (1893).
[2] M. E. Boyd, J. Chem. Phys. **29**, 108 (1958).
[3] A. Pastorek, V. H. J. Clark, S. N. Yurchenko, M. Ferus, and S. Civiš, Spectrochim. Acta, Part A **278**, 121322 (2022).
[4] D. Darby-Lewis, H. Shah, D. Joshi, F. Khan, M. Kauwo, N. Sethi, P. F. Bernath, T. Furtenbacher, R. Tóbiás, A. G. Császár, and J. Tennyson, J. Mol. Spectrosc. **362**, 69 (2019).
[5] S. Civiš, A. Pastorek, M. Ferus, S. N. Yurchenko, and N.-I. Boudjema, Molecules **28**, 3362 (2023).
[6] P. Swings, C. T. Elvey, and H. W. Babcoc, Astrophys. J. **94**, 320 (1941).
[7] R. Meier, D. Wellnitz, S. J. Kim, and M. F. A'Hearn, Icarus **136**, 268 (1998).
[8] D. M. Meyer and K. C. Roth, Astrophys. J. **376**, L49 (1991).
[9] I. A. Crawford and D. A. Williams, Mon. Not. R. Astron. Soc. **291**, L53 (1997).
[10] R. S. Ram, P. F. Bernath, and K. H. Hinkle, J. Chem. Phys. **110**, 5557 (1999).
[11] R. S. Ram and P. F. Bernath, J. Mol. Spectrosc. **260**, 115 (2010).
[12] A. M. Fernando, P. F. Bernath, J. N. Hodges, and T. Masseron, J. Quant. Spectrosc. Radiat. Transfer **217**, 29 (2018).
[13] D. Gupta, K. L. Baluja, and M.-Y. Song, Phys. Plasmas **26**, 063503 (2019).
[14] Y. R. Liu, Y. Wu, J. G. Wang, O. Vendrell, V. Kimberg, and S. B. Zhang, Phys. Rev. Res. **2**, 043348 (2020).
[15] D. R. Yarkony, J. Chem. Phys. **91**, 4745 (1989).
[16] Z. Song, D. Shi, J. Sun, and Z. Zhu, Comput. Theor. Chem. **1093**, 81 (2016).
[17] Y. Zhang, Q. Wang, S. Ni, L. Ji, Z. Cao, and J. Qi, Spectrochim. Acta, Part A **267**, 120578 (2022).
[18] M. Zhou and Z. Zhu, Comput. Theor. Chem. **1204**, 113358 (2021).
[19] L. C. Owono Owono, N. Jaidane, M. G. Kwato Njock, and Z. Ben Lakhdar, J. Chem. Phys. **126**, 244302 (2007).
[20] K. P. Kirby and E. M. Goldfield, J. Chem. Phys. **94**, 1271 (1991).
[21] L. C. Owono Owono, D. Ben Abdallah, N. Jaidane, and Z. Ben Lakhdar, J. Chem. Phys. **128**, 084309 (2008).
[22] A. N. Perri and L. K. McKemmish, Mon. Not. R. Astron. Soc. **531**, 3023 (2024).
[23] S. N. Yurchenko, L. Lodi, J. Tennyson, and A. V. Stolyarov, Comput. Phys. Commun. **202**, 262 (2016).
[24] L. K. McKemmish, C. A. Bowesman, K. Kefala, A. N. Perri, A. M. Syme, S. N. Yurchenko, and J. Tennyson, RAS Tech. Instrum. **3**, 565 (2024).
[25] J. S. A. Brooke, P. F. Bernath, C. M. Western, M. C. van Hemert, and G. C. Groenenboom, J. Chem. Phys. **141**, 054310 (2014).
[26] J. S. A. Brooke, P. F. Bernath, and C. M. Western, J. Chem. Phys. **143**, 026101 (2015).
[27] J. Tennyson, S. N. Yurchenko, J. Zhang, C. A. Bowesman, R. P. Brady, J. Buldyreva, K. L. Chubb, R. R. Gamache, M. N. Gorman, E. R. Guest, C. Hill, K. Kefala, A. E. Lynas-Gray, T. M. Mellor, L. K. McKemmish, G. B. Mitev, I. I. Mizus, A. Owens, Z. Peng, A. N. Perri, M. Pezzella, O. L. Polyansky, Q. Qu, M. Semenov, O. Smola, A. Solokov, W. Somogyi, A. Upadhyay, S. O. M. Wright, and N. F. Zobov, J. Quant. Spectrosc. Radiat. Transfer **326**, 109083 (2024).
[28] M. Pezzella, S. N. Yurchenko, and J. Tennyson, Phys. Chem. Chem. Phys. **23**, 16390 (2021).
[29] M. Pezzella, J. Tennyson, and S. N. Yurchenko, Mon. Not. R. Astron. Soc. **514**, 4413 (2022).
[30] G. B. Mitev, M. Pezzella, C. A. Bowesman, J. Zhang, S. N. Yurchenko, and J. Tennyson, "ExoMol photodissociation cross sections—II: Continuum absorption and predissociation spectra for the hydroxyl radical," Mon. Not. R. Astron. Soc. (submitted 2025).
[31] A. G. Császár, I. Simkó, T. Szidarovszky, G. C. Groenenboom, T. Karman, and A. van der Avoird, Phys. Chem. Chem. Phys. **22**, 15081 (2020).
[32] A. J. F. Siegert, Phys. Rev. **56**, 750 (1939).
[33] V. A. Mandelshtam, H. S. Taylor, V. Ryaboy, and N. Moiseyev, Phys. Rev. A **50**, 2764 (1994).
[34] R. J. Le Roy, J. Quant. Spectrosc. Radiat. Transf. **186**, 167 (2017).
[35] R. J. Le Roy and W.-K. Liu, J. Chem. Phys. **69**, 3622 (1978).
[36] E. Y. Sidky and I. Ben-Itzhak, Phys. Rev. A **60**, 3586 (1999).
[37] N. Moiseyev, Phys. Rep. **302**, 212 (1998).
[38] G. B. Mitev, J. Tennyson, and S. N. Yurchenko, J. Chem. Phys. **160**, 144110 (2024).
[39] H. J. Werner, P. J. Knowles, G. Knizia, F. R. Manby, M. Schütz, P. Celani, W. Györffy, D. Kats, T. Korona, R. Lindh, A. Mitrushenkov, G. Rauhut, K. R. Shamasundar, T. B. Adler, R. D. Amos, A. Bernhardsson, A. Berning, D. L. Cooper, M. J. O. Deegan, A. J. Dobbyn, F. Eckert, E. Goll, C. Hampel, A. Hesselmann, G. Hetzer, T. Hrenar, G. Jansen, C. Köppl, Y. Liu, A. W. Lloyd, R. A. Mata, A. J. May, S. J. McNicholas, W. Meyer, M. E. Mura, A. Nicklass, D. P. O'Neill, P. Palmieri, D. Peng, K. Pflüger, R. Pitzer, M. Reiher, T. Shiozaki, H. Stoll, A. J. Stone, R. Tarroni, T. Thorsteinsson, and M. Wang, *MOLPRO, version 2015.1, a package of ab initio programs*, 2015, http://www.molpro.net.
[40] T. H. Dunning, Jr., J. Chem. Phys. **90**, 1007 (1989).
[41] D. T. Colbert and W. H. Miller, J. Chem. Phys. **96**, 1982 (1992).
[42] S. N. Yurchenko, W. Szajna, R. Hakalla, M. Semenov, A. Sokolov, J. Tennyson, R. R. Gamache, Y. Pavlenko, and M. R. Schmidt, Mon. Not. R. Astron. Soc. **527**, 9736 (2023).
[43] W. P. Reinhardt, Comput. Phys. Commun. **17**, 1 (1979).
[44] M. Pezzella, G. Mitev, S. N. Yurchenko, J. Tennyson, and A. O. Mitrushchenkov, Phys. Chem. Chem. Phys. **26**, 27519 (2024).
[45] S. N. Yurchenko, A. F. Al-Refaie, and J. Tennyson, Astron. Astrophys. **614**, A131 (2018).
[46] W. H. Smith, J. Brzozowski, and P. Erman, J. Chem. Phys. **64**, 4628 (1976).
[47] D. Patel-Misra, G. Parlant, D. G. Sauder, D. R. Yarkony, and P. J. Dagdigian, J. Chem. Phys. **94**, 1913 (1991).
[48] A. N. Heays, A. D. Bosman, and E. F. van Dishoeck, Astron. Astrophys. **602**, A105 (2017).
[49] H. R. Hrodmarsson and E. F. van Dishoeck, Astron. Astrophys. **675**, A25 (2023).
[50] S. N. Yurchenko, H. Williams, P. C. Leyland, L. Lodi, and J. Tennyson, Mon. Not. R. Astron. Soc. **479**, 1401 (2018).
[51] R. J. Le Roy, Y. Huang, and C. Jary, J. Chem. Phys. **125**, 164310 (2006).
[52] W. R. M. Graham and H. Lew, Can. J. Phys. **56**, 85 (1978).
[53] C. R. Brazier, R. S. Ram, and P. F. Bernath, J. Mol. Spectrosc. **120**, 381 (1986).
[54] V. A. Mandelshtam, T. R. Ravuri, and H. S. Taylor, Phys. Rev. Lett. **70**, 1932 (1993).
[55] J. W. Cooley, Math. Comput. **15**, 363 (1961).
[56] J. K. Cashion, J. Chem. Phys. **39**, 1872 (1963).
[57] R. N. Zare, J. Chem. Phys. **40**, 1934 (1964).
[58] W. E. Milne, Phys. Rev. **35**, 863 (1930).
[59] J. N. L. Connor and A. D. Smith, J. Chem. Phys. **78**, 6161 (1983).
[60] R. Baková, J. Fišer, T. Šedivcová-Uhlíková, and V. Špirko, J. Chem. Phys. **128**, 144301 (2008).
[61] T. Šedivcová, V. Špirko, and J. Fišer, J. Chem. Phys. **125**, 164308 (2006).
[62] T. Šedivcová-Uhlíková, P. R. Kaprálová-Žďánská, and V. Špirko, Int. J. Quantum Chem. **107**, 2654 (2007).
[63] R. Püttner, V. Sekushin, H. Fukuzawa, T. Uhlíková, V. Špirko, T. Asahina, N. Kuze, H. Kato, M. Hoshino, H. Tanaka, T. D. Thomas, E. Kukk, Y. Tamenori, G. Kaindl, and K. Ueda, Phys. Chem. Chem. Phys. **13**, 18436 (2011).
[64] B. Jochim, M. Zohrabi, B. Gaire, T. Uhlíková, K. D. Carnes, E. Wells, B. D. Esry, and I. Ben-Itzhak, Phys. Rev. A **104**, 053112 (2021).
[65] B. Jochim, M. Zohrabi, B. Gaire, F. Anis, T. Uhlíková, K. D. Carnes, E. Wells, B. D. Esry, and I. Ben-Itzhak, Phys. Rev. A **105**, 043101 (2022).
[66] I. Simbotin, D. Shu, and R. Côté, Phys. Rev. A **99**, 022709 (2019).
[67] A. Cerioni, L. Genovese, I. Duchemin, and T. Deutsch, J. Chem. Phys. **138**, 204111 (2013).
[68] V. A. Mandelshtam and N. Moiseyev, J. Chem. Phys. **104**, 6192 (1996).
[69] J. A. Gyamfi and T.-C. Jagau, J. Chem. Theory Comput. **20**, 1096 (2024).
[70] U. V. Riss and H. D. Meyer, J. Phys. B: At., Mol. Opt. Phys. **26**, 4503 (1993).
[71] M. Rittby, N. Elander, and E. Brändas, Chem. Phys. **87**, 55 (1984).
[72] Q.-H. Ni, C. Hill, S. N. Yurchenko, M. Pezzella, A. Z. Fateev, Z. Qin, O. Venot, and J. Tennyson, "ExoPhoto: A database of temperature-dependent photodissociation cross sections," RAS Tech. Instrum. (submitted 2025).